Electronic Supplementary Material (ESI) for Soft Matter.

Supporting Information

3D Printing of Complex Origami Assemblages for Reconfigurable Structures

Zeang Zhao[1,2], Xiao Kuang[1], Jiangtao Wu[1], Qiang Zhang[2], Glaucio H. Paulino[3*], H. Jerry Qi[1*], Daining Fang[2,4*]

[1]The George W. Woodruff School of Mechanical Engineering, Georgia Institute of Technology, Atlanta, GA 30332, USA

[2]State Key Laboratory for Turbulence and Complex Systems, College of Engineering, Peking University, Beijing, 100871, P. R. China

[3]School of Civil and Environmental Engineering, Georgia Institute of Technology, Atlanta, GA 30332, USA

[4]Institute of Advanced Structure Technology, Beijing Institute of Technology, Beijing, 100081, P. R. China

Corresponding authors: GHP: paulino@gatech.edu; HJQ: qih@me.gatech.edu; DF: fangdn@bit.edu.cn, or fangdn@pku.edu.cn;

S1. Properties of the photocurable elastomer

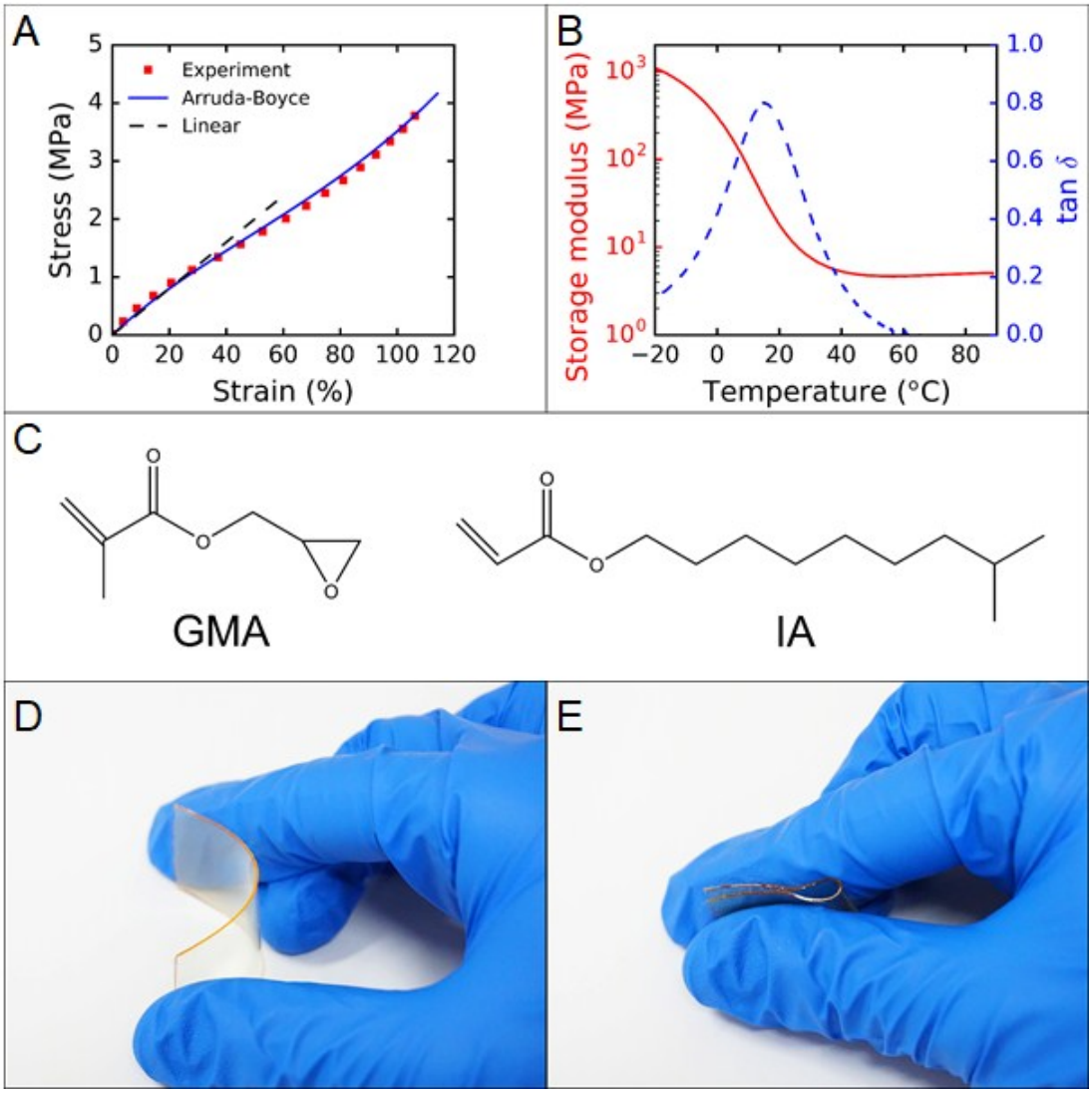

Figure S1. (A) Tensile test of the photocurable elastomer and the comparison with theoretical models. (B) Thermomechanical test of the photocurable elastomer. (C) Chemical structures of GMA and IA monomer. (D)(E) The folding of an photocurable elastomer sheet.

S2. Derivation of the nonlinear beam (NB) theory

Following previous research on the large deformation of curled beams, the equilibrium equations of the beam are [22],

$$\frac{dt_1}{dS} + \kappa t_2 = 0, \tag{S1a}$$

$$\frac{dt_2}{dS} - \kappa t_1 = 0, \tag{S1b}$$

$$\frac{dm}{dS} - \lambda t_2 = 0 . \tag{S1c}$$

The control differential Equation 2 in the main text can be obtained by inserting Equation 1a and Equation 1b into Equation S1c. Because the flat panel attached to the hinge is assumed to be a rigid bar, we transfer the external load P at the end point B to the end point A on the beam (Figure 3B). Thus the effective load at A can be written as,

$$t_{1A} = P\cos\beta_0\cos\theta_A - P\sin\beta_0\sin\theta_A , \tag{S2a}$$

$$t_{2A} = -P\cos\beta_0\sin\theta_A - P\sin\beta_0\cos\theta_A , \tag{S2b}$$

$$m_A = P\sin\beta_0\cos\theta_A L + P\cos\beta_0\sin\theta_A L , \tag{S2c}$$

Where t_{1A} and t_{2A} are components of the internal force at point A, m_A is the moment at point A, β_0 is the initial dihedral angle, L is the length of the rigid bar and θ_A is the incline angle at point A. The internal force at an arbitrary position is related to the force at point A,

$$t_1 = \cos(\theta - \theta_A)t_{1A} + \sin(\theta - \theta_A)t_{2A} , \tag{S3a}$$

$$t_2 = \cos(\theta - \theta_A)t_{2A} - \sin(\theta - \theta_A)t_{1A} \tag{S3b}$$

Inserting Equation S2 and Equation S3 into Equation 2, the following relation is obtained after integration,

$$dS = -\frac{d\theta}{F(\theta)} \tag{S4}$$

With

$$F(\theta)=\sqrt{\frac{2}{EIEA}\sin\left(\frac{\theta-\theta_A}{2}\right)\left[t_{1A}\sin\left(\frac{\theta-\theta_A}{2}\right)-t_{2A}\cos\left(\frac{\theta-\theta_A}{2}\right)\right]}{\left[2EA+t_{1A}\left(1+\cos\left(\theta-\theta_A\right)\right)+t_{2A}\sin(\theta-\theta_A)\right]+\left(\frac{m_A}{EI}\right)^2}}$$

Given an external load P, the corresponding incline angle θ_A at point A could be obtained by solving the equation,

$$L=\int_{\theta_O}^{\theta_A}-\frac{d\theta}{F(\theta)} \tag{S5}$$

Where $\theta_O=\beta_0$ is the incline angle at point O. Coordinates of points on the beam at the deformed configuration can be calculated by,

$$x(\theta)=\int_{\theta_O}^{\theta}-\frac{1}{F(\theta)}\left[\frac{\cos(\theta-\theta_A)t_{1A}+\sin(\theta-\theta_A)t_{2A}}{EA}+1\right]\cos\theta d\theta \tag{S6a}$$

$$y(\theta)=\int_{\theta_O}^{\theta}-\frac{1}{F(\theta)}\left[\frac{\cos(\theta-\theta_A)t_{1A}+\sin(\theta-\theta_A)t_{2A}}{EA}+1\right]\sin\theta d\theta \tag{S6b}$$

While coordinates of points on the rigid bar are related to the coordinates of point A as,

$$x(\mathrm{X})=x_A+X\cos\theta_A \tag{S7a}$$

$$y(\mathrm{X})=y_A+X\sin\theta_A \tag{S7b}$$

Where X is the local coordinate along the rigid bar. The above model was implemented in Matlab to obtain the deformed shapes of the hinge-panel element, as well as the load-displacement curves of the structure.

S3. The assembly method of two adjacent origami tubes

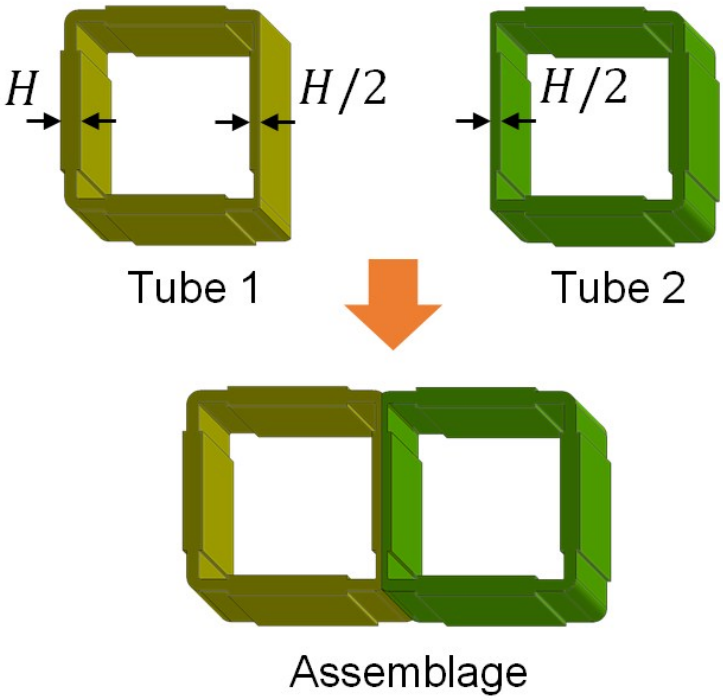

Figure S2. The assembly method of two adjacent origami tubes.

During the assembly of two adjacent origami tubes, the thickness of the panels which will be connected were cut by half (from *H* to *H/2* in Figure S2). As a result, the connection panel in the final assemblage possess the same thickness relative to other panels.

S4. The mechanical reliability of the hinge-panel element

In order to show the mechanical stability of the hinge-panel element, the three special examples with different hinge thicknesses in section 3.3 were further compressed in FEA until the two panels were in parallel. As shown in Figure S3, the maximum stress in the structure is well below the break stress of the elastomer, which is around 4*MPa* in Figure S1A.

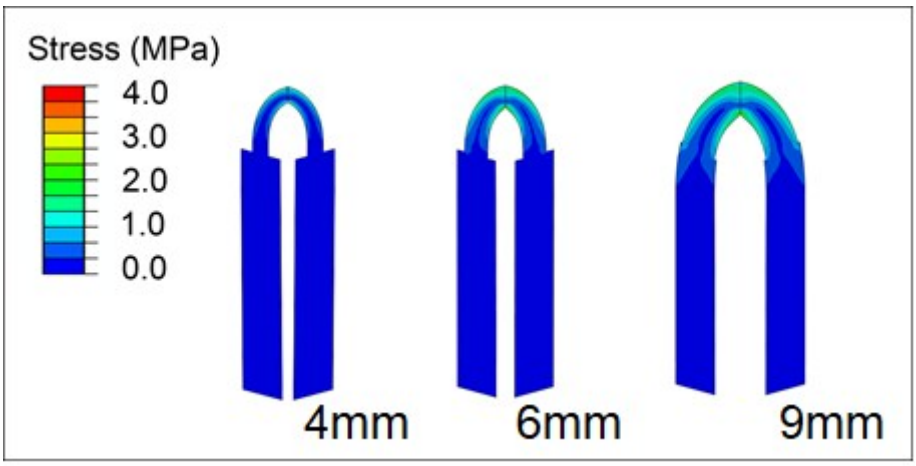

Figure S3. The Mises stress contours of different hinge-panel elements in the folded state (obtained by FEA).

S5. Geometry parameters of 3D printed origami assemblages

Figure	*L*	*l*	*γ*	*α*	*H*	*h*
Fig. 3	6.0	0.8	45	75	1.0	0.4
Fig. 4B	6.0	1.6	45	75	1.0	0.4/0.6/0.9
Fig. 5A	6.0	1.6	45	75	1.0	0.4
Fig. 5B	6.0	1.6	45	75	1.0	0.4
Fig. 6A	6.0	1.6	45	80	1.0	0.4
Fig. 6B	6.0	1.6	45	80	1.0	0.4
Fig. 7A	6.0	1.6	45	75	1.0	0.4
Fig. 7C	6.0	1.6	45	75	1.0	0.4
Fig. 7E	6.0	1.6	45	75	1.0	0.4

L (mm): edge length of the flat panel

l (mm): length of the hinge

γ (°): characteristic angle

α (°): oblique angle of the flat panel

H (mm): thickness of the panel

h (mm): thickness of the hinge

S6. Repeatability of the printed origami assemblages

The reliability of the printed origami assemblages was proved by implementing a set of repeat tests. The compression of the zipper coupled origami tubes was repeated several times, and the force displacement curves are summarized in Figure S2. The mechanical property remained the same after 5 experiment cycles.

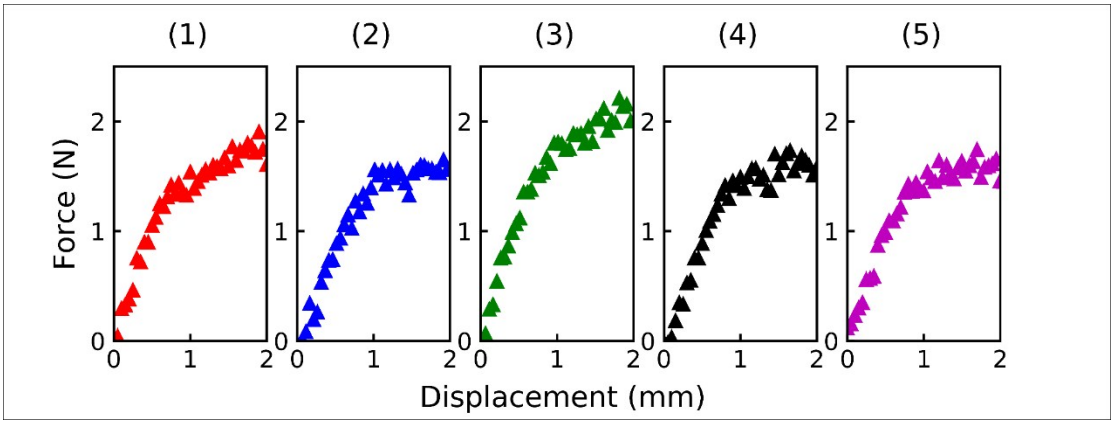

Figure S4. Force displacement curves of the zipper-coupled origami tubes. (hinge thickness 400μm, repeated for 5 times)

S7. Additional information of the printed origami assemblages

Similar to the origami cubes in Figure 5, the origami bridges shown in Figure 6 could be folded to compact shapes. Different folded configurations of the aligned origami bridge and the zipper-coupled origami bridge are shown in Figure S2. Compared with the direct aligning of origami tubes along one direction, the zipper-coupled bridge could be folded to much smaller size (Figure S2C-D), which offers advantage for structures that need to be transported to different locations.

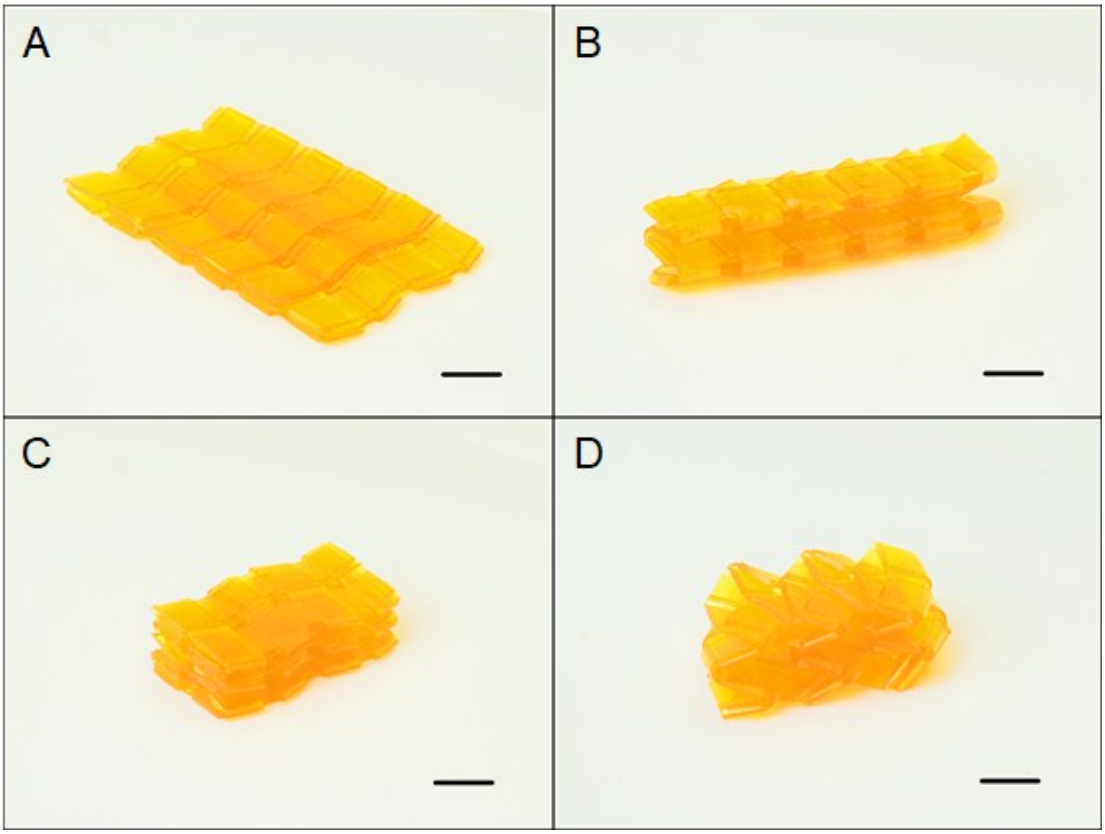

Figure S5. (A) The first folded configuration of the aligned origami bridge. (B) The second folded configuration of the aligned origami bridge. (C) The first folded configuration of the zipper-coupled origami bridge. (D) The second folded configuration of the zipper-coupled origami bridge. (scale bar: 5mm)

S8. Supporting movies

Movie S1. Folding process of the aligned origami tubes and the zipper-coupled origami tubes.

Movies S2. Load capacity of the aligned origami bridge and the zipper-coupled origami bridge.

Movie S3. Folding process of the square/hexagon coupled origami assemblages.